Generator-Sensor Impedance at Double Channel Electrodes

Thomas Holm[a,b], Mats Ingdal[a,b], Jonathan R. Strobl[b], Espen V. Fanavoll[b],
Svein Sunde[a], Frode Seland[a], David A. Harrington[b,*]

[a]*Department of Materials Science and Engineering, Norwegian University of Science and Technology, NO-7491 Trondheim, Norway.*
[b]*Department of Chemistry, University of Victoria, Victoria, British Columbia, V8W 3V6, Canada.*

Abstract

A method for measuring downstream concentration effects through electrochemical impedance spectroscopy at double channel electrodes is demonstrated. An ac current perturbation is applied at an upstream working electrode and the resulting ac potential response at a downstream sensing electrode is measured. This generator-detector scheme is implemented with a single potentiostat. Experimental data for a reversible redox couple are presented and good agreement is found with numerical simulations. A qualitative explanation of the features is given which lays the foundation for a more rigorous theoretical treatment. Relationships with flow rate and frequency are found that can scale the data to lie on a universal curve.

Keywords:
channel electrode, electrochemical impedance spectroscopy, mass transport, FEM

1. Introduction

The simplicity of fabrication offered by soft lithography using polydimethylsiloxane (PDMS) has led to a large increase in the use of microfluidic flow cells in the last decade. For electrochemists, the laminar flow regime offers the possibilities of making membraneless fuel cells [1], membraneless water electrolysers with automatic gas separation [2], and various sensor technologies [3]. A series of electrodes in a microfluidic channel can serve as an electroanalytical tool

---

*Corresponding author. Tel.: +1-250-721-7166

Email addresses: `thomhol@uvic.ca` (Thomas Holm), `mats.ingdal@ntnu.no` (Mats Ingdal), `jrs303@case.edu` (Jonathan R. Strobl), `espen.v.fanavoll@ntnu.no` (Espen V. Fanavoll), `svein.sunde@ntnu.no` (Svein Sunde), `frode.seland@ntnu.no` (Frode Seland), `dharr@uvic.ca` (David A. Harrington)

analogous to the rotating ring-disc electrode (RRDE), with an upstream generator electrode and downstream detector electrodes. Used in this way, channel electrodes allow for more flexible configurations, high collection efficiencies, and use of much smaller amounts of analyte compared to the RRDE.

A mathematical treatment of channel electrodes is more complicated than for the RRDE, as channel electrodes are not uniformly accessible. However, solutions for various kinetics and mass transport problems at a single channel electrode are available including transient current response [4–7] and impedance response [8–11]. For double channel electrode configurations, dc collection efficiency calculations are available for a single species [12–15] and for more complicated reaction mechanisms [16–18]. The case of impedance or frequency response at double channel electrodes has not been treated in the literature, but the analogous RRDE system has been treated by Albery and co-workers where a solution for the ac collection efficiency based on the Laplace transform method was presented [19, 20]. However, numerical approximations were required, and a qualitative analysis as we present below was not attempted.

In this work, an impedance method is described that uses a single potentiostat to apply a current perturbation at an upstream electrode and measure the potential response at a downstream electrode. We define a new quantity, the downstream impedance, Z_{dn}, as the ratio of the ac potential at the downstream sensing electrode (SE) to the ac current density at the upstream working electrode (WE), Eq. (1), where the ac quantities are frequency-dependent complex number phasors in the usual way.

$$Z_{dn} = \frac{\widetilde{E}_{SE}}{\widetilde{j}_{WE}} \tag{1}$$

This quantity was measured for a fast reversible redox couple over a wide range of flow rates, and experimental, numerical, and approximate analytical solutions are compared.

The phase and magnitude of Z_{dn} are given a simple interpretation in terms of an ac concentration wave traveling from the WE to the SE, with the phase related to the time delay and the magnitude related to the diffusive spread across the channel during the travel.

2. Methods

2.1. Microfluidics

The production of the microfluidic cells has been described previously [11]. In short, soft lithography methods were used to make the microfluidic flow cell where the electrodes were vapour deposited onto clean glass slides while the channels were made using PDMS. The geometry of the cell is shown in Fig. 1a, with electrode widths, $w = 100$ μm, channel height, $h = 100$ μm, channel breadth (distance between channel walls perpendicular to flow direction), $d = 1$ mm, and distance between the midpoint of the upstream and downstream electrodes, $l = 200$ μm. For the inlet and outlet, a hole punch was used to

make it possible to fit the inlet teflon tube (OD = 0.51 mm). At the outlet, a reservoir was fitted, all seen in Fig. 1a. The electrolyte was pumped by using a syringe pump (Harvard Apparatus PHD 2000), where the flow rates applied in this work were between 30 and 300 μL min^{-1}.
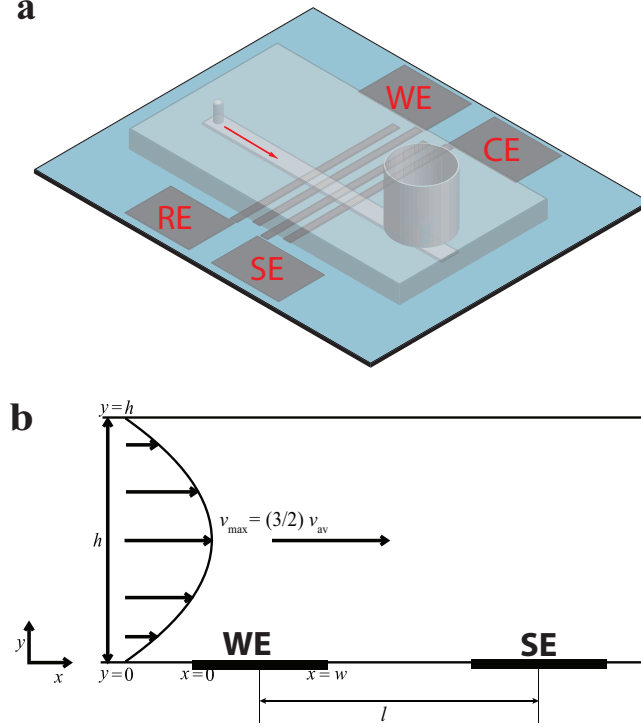

Figure 1: Schematic of the cell (a), and the 2D geometry modelled in this work (b). The arrows indicate the flow direction in the channel and the electrodes are marked as reference electrode (RE), working electrode (WE), sensing electrode (SE), and counter electrode (CE). In (b), flow is from left to right, passing the WE and SE electrodes in the bottom of the channel. The parabolic fluid velocity profile is shown, together with the relationship between the average and maximum velocities.

2.2. Electrochemistry

The preparation and setup is similar to the one reported previously [11]. The aqueous solution was a nominally equimolar (5 mM) mixture of $Ru^{II}(NH_3)_6Cl_2$ and $Ru^{III}(NH_3)_6Cl_3$ in 0.1 M K_2SO_4 electrolyte. The potentiostat used was a Gamry Ref. 600. The first electrode upstream (of a total of four) was the reference electrode (RE), whose potential was established by the Ru(II/III) redox couple. The second electrode was the working electrode (WE), the third electrode was the sensing electrode (SE) and the fourth electrode was the counter electrode (CE), as described in Fig. 1a. The experiment was conducted by running galvanostatic electrochemical impedance spectroscopy (GEIS) with a

100 nA amplitude (rms). The amplitude used was determined by running the experiment and making sure that the resulting potential amplitude at the upstream electrode was less than 10 mV (rms). The working electrode connector was connected to the WE while the working sense connector was connected to the SE to measure the SE potential vs RE. Only a single potentiostat was necessary. The impedance measurements were done under varying flow rates from $30~\mu\mathrm{L}~\mathrm{min}^{-1}$ to $300~\mu\mathrm{L}~\mathrm{min}^{-1}$. The real part of the resulting experimental data was adjusted to ensure that $Z(\omega \to \infty) = 0$.

2.3. Numerical modelling

The mass transport in the channel is approximated by the 2D convective-diffusion equation, Eq. (2) and Fig. 1b, with the flow rate being the fully developed flow $v(y) = 6v_{\mathrm{av}}y(h-y)/h^2$.

$$\frac{\partial c_i}{\partial t} = D_i \frac{\partial^2 c_i}{\partial x^2} + D_i \frac{\partial^2 c_i}{\partial y^2} - v(y)\frac{\partial c_i}{\partial x} \qquad (2)$$

Here, v_{av} is the average velocity in the channel, h is the full channel height, D_i is the diffusivity of species i, c_i is the concentration of species i, t is time, and x and y are the directions parallel and perpendicular to the channel flow direction, respectively. This treatment makes the usual assumptions used for electrode kinetics in supporting electrolytes, e.g., neglect of electric field and double-layer effects. Eq. (2) has to be solved in the electrolyte volume for an applied current perturbation at the working electrode.

A finite element method solver (COMSOL Multiphysics® [21]) was used to numerically solve the 2D problem described above without further simplifications. This model is similar to the one used in our previous work on channel electrodes [11]. However, at the working electrode, the boundary condition used was an oscillating with linear kinetics giving the same ac current as in the experimental work (100 nA(rms)). The downstream electrode has the same boundary condition as the walls, i.e., a zero flux boundary condition. The meshing was based on the ac diffusion length at the highest frequency used (1 kHz), $x_{\mathrm{diff}} = \sqrt{D_{\mathrm{Ru(II)}}f_{\mathrm{max}}^{-1}}$, and was set to 0.1 x_{diff} at the working and sensing electrodes and allowed to grow up to 10 times this value in the channel at a growth rate of 1.05. The software uses the ac current to determine the ac fluxes, and solves for the ac concentration profile. The ac potential at the downstream electrode was then calculated from the linearized (small signal) Nernst equation, Eq. (3), averaged over the electrode surface, and finally used to calculate the impedance according to Eq. (1).

$$\widetilde{E}_{\mathrm{SE}} = \frac{RT}{F}\frac{\widetilde{c}_{\mathrm{Ru^{III}}}}{c_{\mathrm{Ru^{II}},\mathrm{ss}}} - \frac{RT}{F}\frac{\widetilde{c}_{\mathrm{Ru^{II}}}}{c_{\mathrm{Ru^{II}},\mathrm{ss}}} \qquad (3)$$

Here $c_{\mathrm{Ru^{II}},\mathrm{ss}}$ and $c_{\mathrm{Ru^{III}},\mathrm{ss}}$ are the dc concentrations at the electrode surface, which are not necessarily equal to the bulk concentrations, $c_{\mathrm{Ru^{II}}}^{\mathrm{b}}$ and $c_{\mathrm{Ru^{III}}}^{\mathrm{b}}$.

4

3. Results and discussion

3.1. Experimental results and numerical simulation

The experimental downstream impedance (boxes) and the numerically modelled solution (full lines) are shown in Fig. 2. The experimental impedance decreases with increasing flow rate but the features of the impedance response are similar for all flow rates. The flow rate dependence is similar to that of the impedance at a single channel electrode [9–11]. The Nyquist representation, Fig. 2a, shows spirals, similar to those observed on rotating ring-disk electrodes [22]. The magnitude, Fig. 2c, decreases to zero at high frequencies. Simultaneously, the phase angle, Fig. 2b, increases from zero at low frequencies to a maximum of about 3π. At higher frequencies, experimental error leads to uncertainty as to which rotation of the spiral the data belongs, and absolute phases could not be reliably determined.

The numerically modelled solutions (full lines in Fig. 2) indicate firstly that Comsol can successfully be used to model this behavior. Secondly, the numerical solution is better at low frequencies than at high frequencies. Especially, this behavior is visible in the phase angle and magnitude plots (Fig. 2b-c) where, for all flow rates, both the change in magnitude and phase angle starts at lower frequencies in the numerical solution than in the experimental data. Similarly, in the Nyquist representation, Fig. 2a, the modelled data fit well at low frequencies but with significant error in the second and third quadrants. The error at higher frequencies can have many sources such as double-layer charging and migration, and these effects are discussed in more detail in Section 3.4.

3.2. A qualitative explanation of downstream impedance

The essential features of the impedance spectra can be understood readily with some simple principles. From here on, we simplify by assuming that the diffusivities are equal and therefore the principle of total unchanging concentration applies [23, 24]. That is, $c_{\mathrm{Ru^{III}}} + c_{\mathrm{Ru^{II}}} = \text{constant}$, and $\widetilde{c}_{\mathrm{Ru^{III}}} = -\widetilde{c}_{\mathrm{Ru^{II}}} = \widetilde{c}$. This reduces the linearized Nernst equation, Eq. (3), to Eq. (4), and implies that the potential at the SE is a scaled version of the ac concentration at its surface and is in phase with it.

$$\widetilde{E}_{\mathrm{SE}} = \frac{2RT}{Fc_{\mathrm{ss}}}\widetilde{c}_{\mathrm{SE}} \qquad (4)$$

The key quantity in interpreting the data is the ac concentration relation between the sensing and the working electrode, $\widetilde{c}_{\mathrm{SE}}/\widetilde{c}_{\mathrm{WE}}$, which may be related to the experimental downstream impedance, Z_{dn} by Eq. (5).

$$Z_{\mathrm{dn}} = \frac{\widetilde{E}_{\mathrm{SE}}}{\widetilde{j}_{\mathrm{WE}}} = \left(\frac{\widetilde{E}_{\mathrm{SE}}}{\widetilde{c}_{\mathrm{SE}}}\right)\left(\frac{\widetilde{c}_{\mathrm{SE}}}{\widetilde{c}_{\mathrm{WE}}}\right)\left(\frac{\widetilde{c}_{\mathrm{WE}}}{\widetilde{j}_{\mathrm{WE}}}\right) \qquad (5)$$

The first factor in Eq. (5), $\widetilde{E}_{\mathrm{SE}}/\widetilde{c}_{\mathrm{SE}}$, is constant, as follows from Eq. (4). The third factor, $\widetilde{c}_{\mathrm{WE}}/\widetilde{j}_{\mathrm{WE}}$, is proportional to the known mass transport impedance
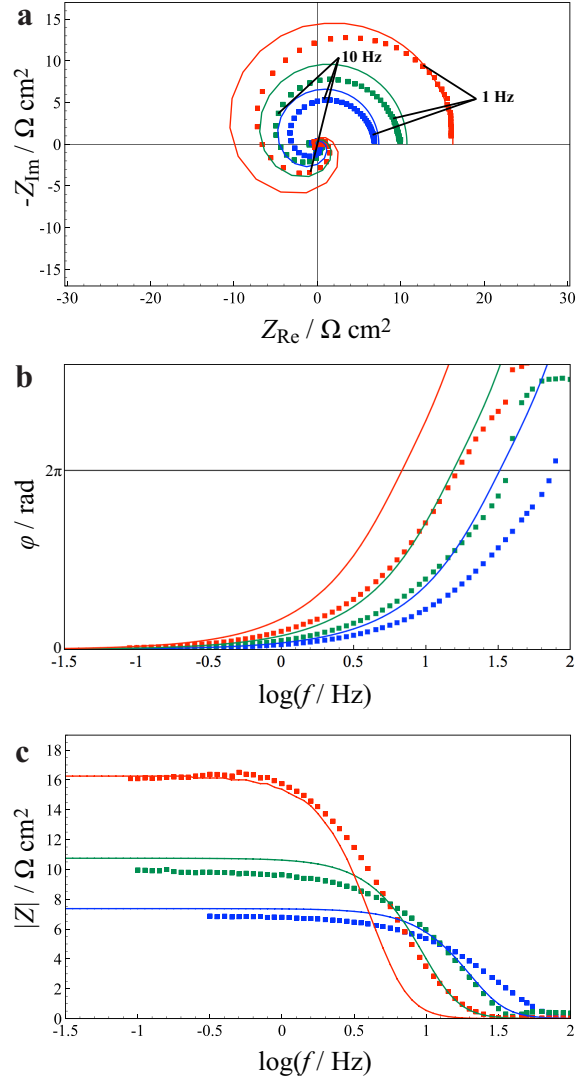
Figure 2: Experimental data (boxes) and numerical model (full lines). Flow rates of 30 μL min^{-1}(red), 100 μL min^{-1}(green), and 300 μL min^{-1}(blue). The data are presented as an impedance plane plot (a), a phase angle vs the logarithm of the frequency representation (b), and a magnitude vs the logarithm of the frequency representation (c).

at a single channel electrode. The phase of the mass transport impedance at a channel electrode is in the low range $0 - \pi/4$ [9–11], and a closer examination (c.f. Fig. 4, Ref. 11) shows that except at the lowest frequencies, the total phase angle of the downstream impedance is dominated by the phase of $\widetilde{c}_{SE}/\widetilde{c}_{WE}$.

The phase relationship between the WE and the SE can be understood in terms of the time spent in the channel by a concentration wave that is traveling downstream at an averaged velocity, v_{wave}. This concentration wave is sensed at the downstream electrode and the phase depends on the distance between the electrodes, l, the velocity, v_{wave}, and the frequency, f. Such a concentration wave is illustrated in Fig. 3, where two cases, (a) and (c), are examples where the WE and SE concentrations are in-phase and represent two full or four full wavelengths between the electrodes. The last case (b) is a case where 2.5 full wavelengths are between the electrode midpoints resulting in a fully out-of-phase response (real negative value). This leads to the simple criterion for in-phase response given in Eq. (6), where n is the number of full rotations. Of course, these in-phase and out of phase relationships are part of a continuum.
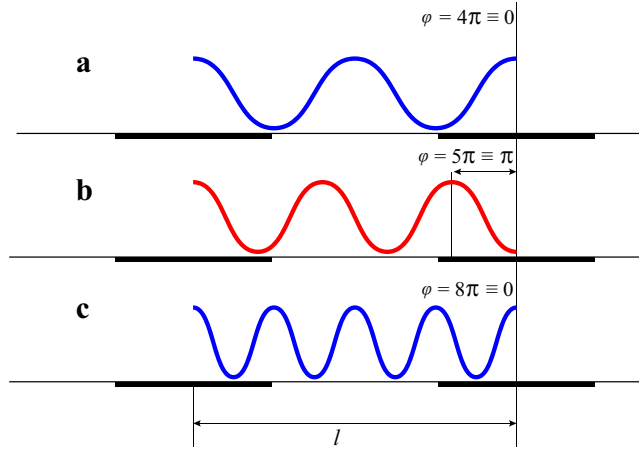

Figure 3: Figure demonstrating the principle of in-phase and out of phase concentrations. The examples given are for in-phase concentration with $n = 2$ (a), out-of-phase concentration with $n = 2$ (b), and in-phase concentration with $n = 4$ (c). Examples a and c result in a real positive impedance, while example b results in a real negative impedance.

$$f = \frac{n v_{wave}}{l} \tag{6}$$

Eq. (6) can be derived mathematically if one ignores the diffusion terms in the convective-diffusion equation, Eq. (2), and approximates the velocity as independent of y, i.e., $v(y) = v_{wave}$. The simplified equation is then converted to small-signal form, Eq. (7), and solved to find that the phase delay changes linearly with x, Eq. (8).

$$i\omega\widetilde{c}(x) = v_{\text{wave}}\frac{d\,\widetilde{c}(x)}{d\,x} \tag{7}$$

$$\widetilde{c}(x) = \widetilde{c}(0)\exp\left(\frac{i\omega x}{v_{\text{wave}}}\right) \tag{8}$$

The phase at $x = l$ relative to that at $x = 0$, $\omega l/v_{\text{wave}}$, divided by 2π is the number of rotations n, and we recover Eq. (6). This prediction of the phase changing linearly with frequency is shown in Fig. 4 to be approximately true for the data at 100 μL min^{-1}. The accompanying decrease in magnitude is attributed to diffusive spread across the channel, which weakens the coherence of the wave, as the real velocities are different for different distances from the bottom of the channel. The linear increase in phase with frequency combined with the slow decrease in magnitude with frequency explains the spiral shapes in the spectra.
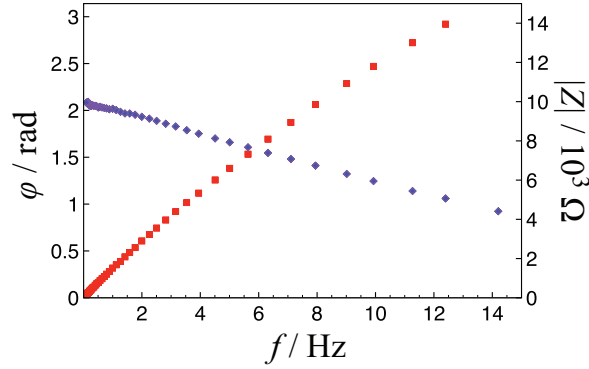

Figure 4: Figure showing the angle (blue diamonds) and magnitude (red rectangles) vs the frequency for the frequencies in the first half round of the spiral for the 100 μL min^{-1} experimental data.

The simple explanation based on Fig. 3 assumes there is a unique concentration across the whole of the SE surface. However, at higher frequencies, the combination of frequency and the flow rate yields cases where several wavelengths pass over the SE surface. This will give a perturbing concentration over the electrode resulting in a very small total potential when average by using Eq. (3). This leads to a breakdown of the simple explanation, which may contribute to the deviation from linear phase behaviour and contribute to the decrease in magnitude. At higher frequencies the assumption of a zero-flux boundary condition and an averaged Nernstian response may break down due to kinetic or double-layer charging effects.

3.3. Flow rate and frequency dependence

Inspection of Fig. 2 suggests that the impedances might lie on a commmon curve if the frequencies and magnitudes were appropriately scaled by a function

of flow rate. Limiting currents at channel electrodes scale as the cube root of sweep rate, which suggests a cube root dependence might be appropriate here. The cube root dependence is an outcome of making the common assumptions that axial diffusion (in the x direction) may be neglected and that the flow velocity may be approximated as proportional to y (the Lévêque approximation). The simplified Eq. (2) then gives the small-signal Eq. (9).

$$i\omega\widetilde{c} = D\frac{\partial^2\widetilde{c}}{\partial y^2} - \frac{6v_{\mathrm{av}}y}{h}\frac{\partial\widetilde{c}}{\partial x} \tag{9}$$

The changes of variables $X = x/w$, $\widetilde{C} = \widetilde{c}/c^{\mathrm{b}}$, $Y = \sqrt{\omega/D}y$, and $\Omega = (h^2w^2/36v_{\mathrm{av}}^2D)^{1/3}\omega$ give the dimensionless Eq. (10).

$$i\widetilde{C} = \frac{\partial^2\widetilde{C}}{\partial Y^2} - \frac{Y}{\Omega^{3/2}}\frac{\partial\widetilde{C}}{\partial X} \tag{10}$$

This suggests that the ac concentration and quantities derived from it must be functions of $\Omega^{3/2}$ (or of Ω itself), in which the flow rate appears to a $1/3$ power.

Complete solution of this equation is nontrivial, but it is possible to solve it at zero frequency for the constant ac flux boundary condition, which can then be used to find the zero-frequency downstream impedance. In the literature, the equivalent steady-state problem has been treated for the case of constant concentration (collection efficiency) [12, 13, 15] and for the case of irreversible kinetics at the electrode surface [25, 26]. However, the constant flux solution, although much used in work on rotating ring-disc electrode [27–29], has to the best of our knowledge not been solved for the channel electrode geometry.

Experimentally, an imposed constant ac current at the WE need not imply that the ac flux is the same over the electrode surface [30], but a boundary condition of constant ac flux across the electrode surface proves to explain the results well. In the appendix, this boundary condition is used to find the ac concentration along the bottom of the channel and thence the low frequency limit of the downstream impedance, Eq. (11).

$$Z_0 = \frac{2RT}{n^2F^2Dc^{\mathrm{b}}\widetilde{J}(X_3 - X_2)}\left(\frac{Dhw}{6v_{\mathrm{av}}}\right)^{1/3}\int_{X_2}^{X_3}\widetilde{C}(X,0)dX \tag{11}$$

Here, $\widetilde{J} = (\widetilde{j}/nFDc^{\mathrm{b}})(Dhw/6v_{\mathrm{av}})^{1/3}$ is the dimensionless ac current applied, c^{b} is the bulk concentration, $X = x/w$, and X_2 and X_3 are the upstream and downstream edges of the SE.

This zero frequency impedance can be compared with the numerical solutions at different flow rates to check if the assumptions in the derivation, i.e., absence of axial diffusion and the Lêvéque approximation, are valid. This is similar to the approach used in our previous work on mass transport impedance at a single channel electrode [11]. For the cell geometry used here, the analytical solution was found to be within 10% of the full numerical solution for flow rates equal to or higher than 10 μL min^{-1}. This result also indicates that the assumption

9

that the flux is constant across the WE surface gives a solution similar to the constant total current boundary condition applied experimentally.

The experimental impedances are normalized by dividing by Z_0 and are plotted as a function of Ω in Fig. 5. The experimental data fall on a universal curve in all cases except at low frequencies for the 30 μL min^{-1} flow rate. This anomaly in the 30 μL min^{-1} is likely an experimental artefact due to the slow deterioration of the redox couple when small amounts of oxygen are present in the solution. The numerical solutions also fall on a common curve, and are in good agreement with experiment. As expected, the scaling relationships for flow rate and frequency in Z_0 and Ω correctly describe the mass transport in the channel. In particular the magnitude of the downstream impedance is proportional to the cube root of the flow rate, $v_{\mathrm{av}}^{1/3}$.

With this scaling relationship in hand, we revisit the suitability of the linear phase approximation for all flow rates. Fig. 6 shows the logarithm of the phase angle vs the logarithm of Ω for the numerical and experimental data. Two domains can be distinguished. For $\Omega < 1$, the slope of the curve is 1 as expected from our simple treatment above. Given that this model completely neglects diffusion, it is remarkably successful.

For $\Omega > 1$, the slope decreases both for the experimental and numerical data. As already discussed, the averaging over the SE electrode likely contributes to this. This is also the region where diffusion across the channel becomes significant compared to convection. It is unlikely that the spread of molecules across the channel to locations with different downstream velocities can be simply treated.

3.4. Effects at high frequencies

In this section we consider effects beyond those used in the simulations in order to investigate the discrepency between the model and experiment at higher frequencies. At higher frequencies, double-layer charging currents become more significant. At the SE, the net current is zero, and double-layer charging could be balanced by an equal and opposite faradaic current. The consideration of faradaic current implies that the finite reaction rate needs to be considered, which is characterized by the charge-transfer resistance. Allowing the faradaic and changing currents to oscillate causes a deviation from the proportional relationship between oscillating concentration and potential given by Eq. (4), which may be estimated by Eq. (12)

$$\widetilde{E} = \widetilde{E}_{\mathrm{rev}} \left(1 + \mathrm{i}\,\omega C_{\mathrm{dl}} R_{\mathrm{ct}}\right)^{-1} \tag{12}$$

The time constant $C_{\mathrm{dl}} R_{\mathrm{ct}}$ estimated from the small semicircle in the impedance at the WE corresponds to a frequency of about 10 kHz, and so this correction is neglible at the much lower frequencies where the modelled and experimental downstream impendances deviate.

Solution resistance effects may be estimated in a similar fashion. Although the resistance between two electrodes can be high, the electrode area is low and R_{s} has a typical value of about 1 Ω cm^2. This is comparable to R_{ct}, and so the
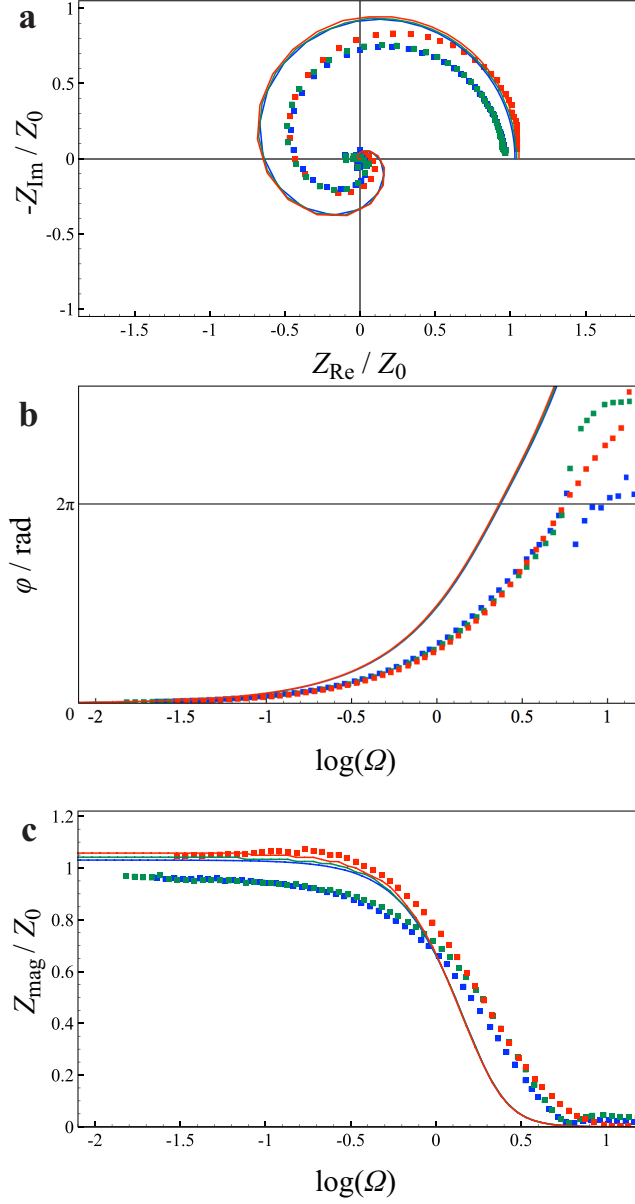
Figure 5: Experimental and numerically calculated data for all flow rates shown as normalized impedance, Z/Z_0. The data is shown as an impedance plane plot (a), as phase angle vs the logarithm of the dimesionless frequency, Ω (b), and as normalized magnitude vs the logarithm of the dimensionless frequency, Ω (c). The experimental values are shown as boxes, while the numerical results calculated using Comsol are shown as full lines. The flow rates are 30 μL min^{-1} (red), 100 μL min^{-1} (green), and 300 μL min^{-1} (blue).
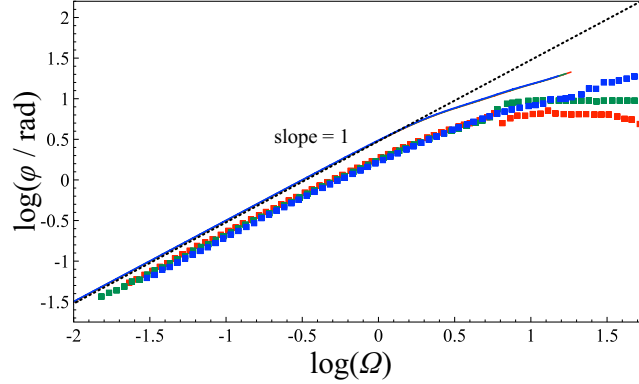
Figure 6: Logarithm of the phase angle vs the logarithm of the dimensionless frequency, Ω, for the experimental values (boxes) and the numerical solutions (full lines). Flow rates of 30 μL min^{-1}(red), 100 μL min^{-1}(green), and 300 μL min^{-1}(blue). The dotted trend line has a slope of 1.

effects should appear at similarly high frequencies. In the approximation that the migration and convective-diffusive problems are uncoupled, this manifests only in a real part offset to the downstream impedance.

These effects are estimated on the assumption that the SE does not interact with the concentration field generated by the WE or the electric field generated by the WE and CE. Other more subtle effects dependent on coupling between migration, diffusion and reaction are possible, such as local faradaic currents induced at the SE by the bipolar effect [31], or significant current carried by the reactants or products. These effects, including extension to 3-D modelling. will be considered in future work in the context of quasireversible kinetics. We note, however, that the impedance at the WE is accurately modelled within the present framework [11]. The fact that the normalized downstream impedances fall on a common plot against Ω (Fig. 5) also argues that convective-diffusive effects dominate over migration effects.

4. Conclusion

A new measurement technique, downstream electrochemical impedance spectroscopy, Z_{dn}, is described. In this technique, the current at an upstream electrode is modulated and the resulting modulation in the concentration is detected at a downstream high-impedance sensor electrode.

The technique is described and experimentally tested for the case of a reversible redox couple in solution. The Nyquist plots show spirals. Numerical simulations were used to verify the results, and a simple qualitative analysis is given for the phase dependence. Analytical approaches show that this is the correct first-order explanation of the phase. An exact solution for the ac concentration dependence along the bottom of the channel between electrodes is given, under the assumption that axial diffusion may be neglected and the Lêvéque

12

approximation applies. The flow rate dependence is analyzed and the influence of the frequency and the convection on the concentration distribution can be understood through a dimensionless frequency parameter Ω. Despite being an upstream-generation/downstream-detection method, it was implemented using only one potentiostat. The method is most useful for relatively small electrodes compared to the distance between them, and for higher flow rates.

An exact solution is given for the zero-frequency limit of the downstream impedance, which agrees with experiment, and could therefore be used to determine unknown experimental parameters such as flow rate. Future development of the method may enable measurement of rate constants for homogenous reactions in the channel, in a similar manner to conventional collection efficiency experiments.

5. Acknowledgements

Appendix A. Derivation of zero-frequency downstream impedance

The ac concentration of a generated species downstream along the bottom of the channel can be found by solving the ac convective-diffusion equation, Eq. (9), which neglects axial diffusion and makes the Lêvéque approximation. It is solved only for the low-frequency limit ($\omega \to 0$), i.e., the left-hand side is set to zero. By changing variables to $X = x/w$, $Y = (6v_{av}/Dhw)^{1/3}y$, and $\widetilde{C} = \widetilde{c}/c^b$, we get the dimensionless Eq. (A.1). Note that Y here is different from Y in Eq. 10.

$$0 = \frac{\partial^2 \widetilde{C}}{\partial Y^2} - Y\frac{\partial \widetilde{C}}{\partial X} \tag{A.1}$$

The ac concentration is zero upstream of the WE, $\widetilde{C}(0, Y) = 0$, and far above the electrode, $\widetilde{C}(X, Y \to \infty) = 0$. The imposed ac current density at the WE, $\widetilde{j}$, in dimensionless form becomes $\widetilde{J} = (\widetilde{j}/nFDc^b)(Dhw/6v_{av})^{1/3}$. The flux at the bottom of the channel downstream of the WE ($X > 0$) is zero, and this can be combined with the flux at the WE to give a single boundary condition $(\partial \widetilde{C}/\partial Y)|_{Y=0} = \widetilde{J}(1 - H(X - 1))$, where $H(x)$ is the Heaviside function.

Taking the Laplace transform with respect to X and using the $\widetilde{C}(0, Y) = 0$ boundary condition gives Eq. (A.2)

$$0 = \frac{d^2\overline{C}(s,Y)}{dY^2} - Ys\overline{C}(s,Y) \tag{A.2}$$

The general solution is a linear combination of the Airy Ai and Bi functions, and the requirement that the solution is zero at $Y = \infty$ means that the Bi function does not contribute. That is, the solution is

$$\overline{C}(s,Y) = a\mathrm{Ai}(s^{1/3}Y) \tag{A.3}$$

where a is to be determined by the flux boundary condition at $Y = 0$, which in transformed form is $(\partial\overline{C}/\partial Y)|_{Y=0} = \widetilde{J}(1 - \exp(-s))/s$. Applying this boundary condition, solving for a and then setting $Y = 0$ gives the surface concentration in Eq. (A.4).

$$\overline{C}(s,0) = \frac{2(1 - \exp(-s))\widetilde{J}\pi 3^{1/6}}{s^{4/3}3\Gamma(2/3)^2} \tag{A.4}$$

The inverse Laplace transformation of Eq. (A.4) gives the concentration profile along the bottom of the channel, Eq. (A.5).

$$\frac{\widetilde{C}(X,0)}{\widetilde{J}} = \begin{cases} \frac{3^{2/3}}{\Gamma(2/3)}X^{1/3}, & \text{for} \quad 0 \leq X \leq 1 \\ \frac{3^{2/3}}{\Gamma(2/3)}\left(X^{1/3} - (X-1)^{1/3}\right), & \text{for} \quad X \geq 1 \end{cases} \tag{A.5}$$

Averaging over the SE (from X_2 to X_3) and converting to a dimensioned impedance gives the zero frequency downstream impedance of Eq. (11).

References

[1] E. Kjeang, N. Djilali, D. Sinton, Journal of Power Sources 186 (2009) 353–369.

[2] S. M. H. Hashemi, M. A. Modestino, D. Psaltis, Energy & Environmental Science 8 (2015) 2003–2009.

[3] D. G. Rackus, M. H. Shamsi, A. R. Wheeler, Chemical Society Reviews 44 (2015) 5320–5340.

[4] J. Anderson, S. Moldoveanu, Journal of Electroanalytical Chemistry and Interfacial Electrochemistry 179 (1984) 107–117.

[5] S. Moldoveanu, J. Anderson, Journal of Electroanalytical Chemistry and Interfacial Electrochemistry 185 (1985) 239–252.

[6] D. K. Cope, C. H. Scott, V. Kalapathy, D. E. Tallman, Journal of Electroanalytical Chemistry and Interfacial Electrochemistry 280 (1990) 27–35.

[7] C. Deslouis, B. Tribollet, M. A. Vorotyntsev, Journal of The Electrochemical Society 138 (1991) 2651–2657.

[8] R. G. Compton, G. R. Sealy, Journal of Electroanalytical Chemistry and Interfacial Electrochemistry 145 (1983) 35–41.

[9] R. G. Compton, M. E. Laing, P. R. Unwin, Journal of Electroanalytical Chemistry and Interfacial Electrochemistry 207 (1986) 309–314.

[10] R. G. Compton, J. Winkler, Journal of Physical Chemistry 99 (1995) 5029–5034.

[11] T. Holm, M. Ingdal, E. V. Fanavoll, S. Sunde, F. Seland, D. A. Harrington, Electrochimica Acta 202 (2016) 84–89.

[12] R. Braun, Journal of Electroanalytical Chemistry 19 (1968) 23–35.

[13] H. Matsuda, Electroanalytical Chemistry and Interfacial Electrochemistry 16 (1968) 153–164.

[14] K. Aoki, K. Tokuda, H. Matusda, Journal of Electroanalytical Chemistry 195 (1985) 229–249.

[15] C. Brett, A. Oliveira-Brett, E. C. Bamford, E. R. Compton, Comprehensive Chemical Kinetics, volume 26, Elsevier, pp. 355–441.

[16] K. Aoki, K. Tokuda, H. Matsuda, Journal of Electroanalytical Chemistry 79 (1977) 49–78.

[17] A. C. Fisher, R. G. Compton, Journal of Applied Electrochemistry 21 (1991) 208–212.

[18] J. Cooper, R. Compton, Electroanalysis 10 (1998) 141–155.

[19] W. J. Albery, J. S. Drury, M. L. Hitchman, Transactions of the Faraday Society 67 (1971) 161–165.

[20] W. J. Albery, A. H. Davis, A. J. Mason, Faraday Discussions of the Chemical Society 56 (1973) 317–329.

[21] Comsol Inc, COMSOL Multiphysics v 5.1 http://www.comsol.com, 2015. Burlington, MA.

[22] C. Gabrielli, M. Keddam, F. Minouflet-Laurent, H. Perrot, Electrochemical and Solid-State Letters 3 (2000) 418–421.

[23] K. B. Oldham, S. W. Feldberg, Journal of Physical Chemistry B 103 (1999) 1699–1704.

[24] P. A. Kottke, A. G. Fedorov, Journal of Physical Chemistry B 109 (2005) 16811–16818.

[25] Y. V. Tolmachev, Z. Wang, D. Scherson, Journal of the Electrochemical Society 143 (1996) 3160–3166.

[26] Y. V. Tolmachev, Z. Wang, D. Scherson, Journal of the Electrochemical Society 143 (1996) 3539–3548.

[27] W. J. Albery, Transactions of the Faraday Society 62 (1966) 1915–1919.

[28] W. J. Albery, S. Bruckenstein, Transactions of the Faraday Society 62 (1966) 1920–1931.

[29] W. J. Albery, M. L. Hitchman, Ring-Disc Electrodes, Oxford University Press, London, 1971.

[30] M. Fleischmann, S. Pons, Journal of Electroanalytical Chemistry and Interfacial Electrochemistry 250 (1988) 277–283.

[31] T. M. Braun, D. T. Schwartz, Journal of The Electrochemical Society 163(13) (2016) E354–E362.